Spectral Tuning of Organic Nanocolloids

C.M. Spillmann, J. Naciri, G.P. Anderson,
M. Chen, and B.R. Ratna
Center for Bio/Molecular Science and Engineering

Introduction: There is a need within the Navy and Department of Defense for the development of multifunctional and smart materials on the nanoscale. Such materials are relevant to several focus areas of importance to the Navy, including the advancement of nanoscience technology and chemical and biological detection. As part of this vision, NRL is studying the controlled self-assembly and interaction of molecules to create tunable and functional organic nanostructures. Liquid crystal (LC) is a mesophase of matter ideal for incorporating tunable functionality at different length scales due to its ability to inherently self-organize. We use the self-assembly of polymerizable LCs to control the molecular aggregation of stable fluorescent chromophores to create a unique class of organic fluorescent nanocolloids (FNCs) and demonstrate tuned fluorescent emission spectra of nanocolloid populations under single wavelength excitation.

Nanocolloid Synthesis and Characterization: Fluorescent nanocolloids are synthesized using three components: an LC cross-linking agent that exhibits a stable nematic phase, a homologue of the organic chromophore perylene, and polymerizable surfactant. The perylene derivative, PERC11, is chosen due to its strong absorption and fluorescence, and outstanding (photo)chemical and thermal stability. The surfactant capping agent has a carboxylic head group that allows for chemical coupling of the FNC surface to biomolecules of interest. The end result is FNCs composed of a cross-linked network of LC molecules with controlled dye aggregates distributed throughout the interior of the nanocolloid and capped by a functional surfactant.

Using an established two-phase miniemulsion procedure, stable spherical nanocolloids suspended in water are produced with diameters ranging from 50 to 300 nm, as determined from dynamic light scattering and scanning electron imaging. The mole ratio of dye to LC cross-linking agent is varied from 0.6% to 4.8%, and yet within this small range we are able to tune the fluorescent emission of the FNCs over much of the visible spectrum (Fig. 1).

Spectroscopic Characterization: The absorption spectra of FNCs containing 0.6 and 4.8 mol% PERC11 reveal a shift from the 0–0 vibronic transition to the 0–1 and 0–2 transitions of the dye as it assembles into larger aggregates. We also observe a red-shift in the fluorescent emission spectrum as the dye concentration is increased in FNC populations excited at 488 nm. This effect is the result of a shift in the vibronic states of the dye aggregate due to the stacking of the π–π molecular orbitals. Confocal images of four different FNC populations deposited on a substrate demonstrate the tuned emission spectra of the FNCs [Fig. 2(a)]. Spectral analysis of individual colloids reveals that the PERC11 molecular aggregates at a given concentration are uniformly distributed throughout the FNC population [Fig. 2(b)].

Control experiments with non-LC cross-linking agents reveal that control of PERC11 aggregation in

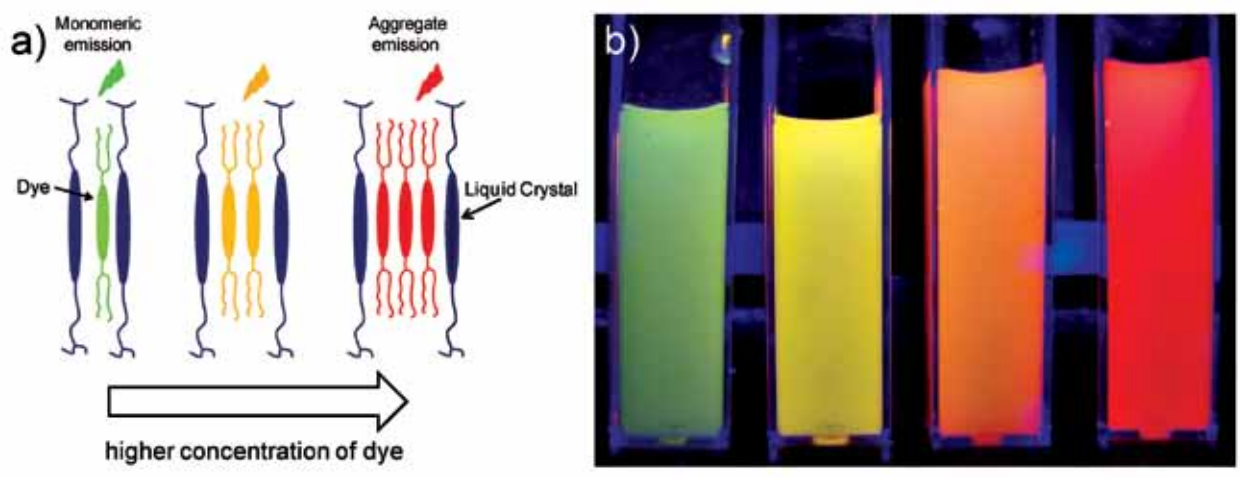

FIGURE 1
(a) Schematic of dye and cross-linking agent interaction. Control of PERC11 aggregation in FNCs is dictated by the ratio of dye to the nematic cross-linking agent DACTP11. A low ratio of dye to DACTP11 results in a monomeric emission spectrum, while increasing the ratio leads to aggregate formation and a red-shift in the emission spectrum. (b) Four FNC populations suspended in water under UV excitation with 0.62 (green), 1.54 (yellow), 2.54 (orange), and 4.84 (red) mol% of PERC11 to DACTP11.

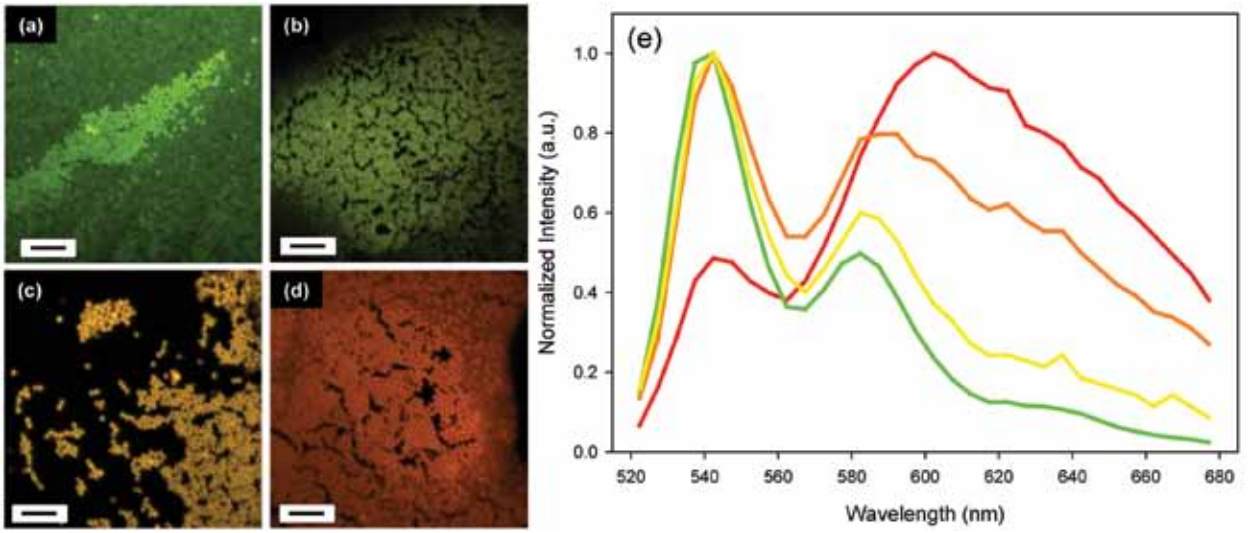

FIGURE 2
Confocal images and emission spectra of FNC samples deposited and dried on silicon substrate correspond to FNC samples with (a) 0.62, (b) 1.54, (c) 2.54, and (d) 4.84 mol% PERC11. (e) Average spectral emission of FNCs in images (a) through (d). Scale bars in images (a) through (d) equal 2 μm.

FNCs is driven by three parameters. The first is miscibility of the molecular components in the temperature range used to synthesize the nanocolloids. The second parameter is π–π molecular interactions between the dye and the LC cross-linking molecule. Our results show that a liquid crystal molecule with sufficient core-core interactions with perylene controls the aggregation of dye molecules. The third parameter is the ratio of the molecular species. Adjusting the mole ratio of PERC11 relative to the LC cross-linker controls the dye aggregation and tunes the fluorescent emission spectra of FNCs. The quantum yield of the FNCs varied from ~1.0 to 0.6 as the emission spectra shifted from green to red, respectively, and indicates that confinement of the dye and dye aggregates by the LC cross-linking agent does not significantly alter with quantum yield in the FNCs.

Fluorescent Tracer in Bioassays: To demonstrate the functionality of FNCs, we bioconjugate the surface to primary amines of NeutrAvidin (NA). The FNC-NA complexes are used as fluorescent tracers in a fluid

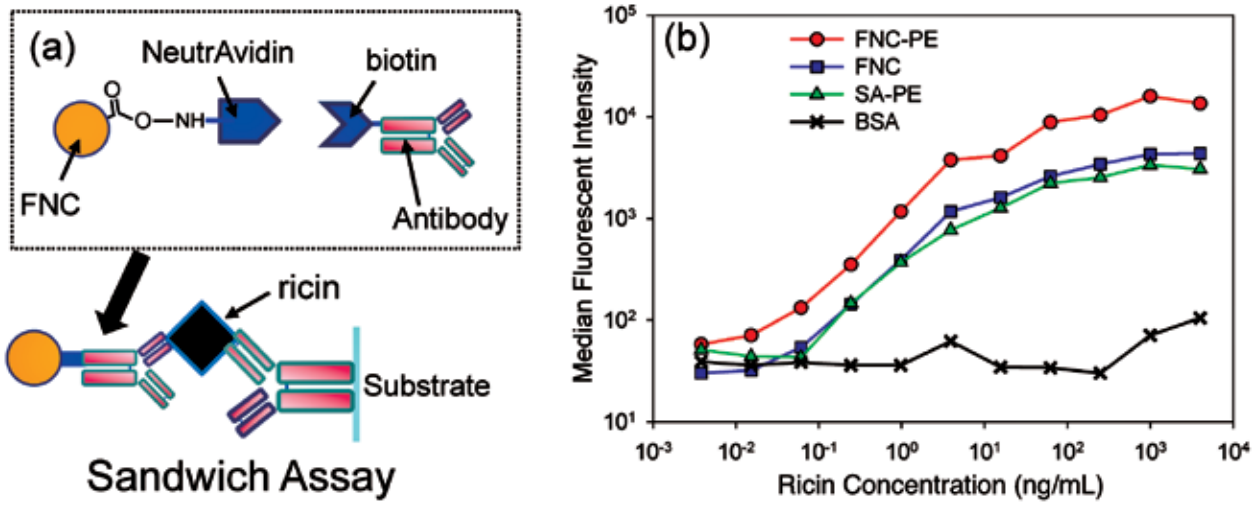

FIGURE 3
Fluid array immunoassay with FNCs. (a) Schematic representation of FNC-NA coupling to biotinylated anti-ricin antibody to complete a sandwich immunoassay. (b) Intensity of FNC-NA conjugated to anti-ricin antibodies tracked as a function of ricin concentration. FNCs (blue) matched signal strength of standard streptavidin-phycoerythrin (SA-PE) bound to anti-ricin (green). Fluorescent intensity of FNC-NAs amplified by addition of biotinylated phycoerthrin (FNC-PE) to NeutrAvidin on a nanocolloid surface (red). Microspheres coated with bovine serum albumin (BSA) were included as control for nonspecific binding (black).

array immunoassay to detect the highly toxic protein ricin. A schematic setup of the FNC preparation and assay is shown in Fig. 3(a). The FNCs match the fluorescent intensity for streptavidin-phycoerythrin (SA-PE), a standard label for the assay [Fig. 3(b)]. The utility of using nanoparticles as a scaffold to amplify the assay is demonstrated by subsequent addition of biotinylated PE (Bt-PE), which upon binding to the unoccupied NA on the nanoparticles results in a four-fold increase in fluorescent intensity. These encouraging initial results portend the usefulness of FNCs in a wide range of fluorescent bioassays.

Summary: We demonstrate the concentration-dependent spectral tuning of perylene in a nanocolloid system. Manipulation of π–π molecular orbital interactions in the presence of an LC component controls the dye stacking and emission spectrum. We find that the molecular structure of the LC cross-linking agent and its phase behavior play a critical role in controlling the perylene molecular aggregates. The organic nanocolloids are highly fluorescent, exhibit a long shelf life, and are easy to bioconjugate. The simplicity of the synthetic approach and ease of surface functionalization provide opportunity to design other novel multifunctional nanocolloids beyond the FNCs described here.

[Sponsored by NRL and DTRA]

Spin Rotation for Quantum Information

S.E. Economou,[1] A. Greilich,[2] and T.L. Reinecke[1]
[1] *Electronics Science and Technology Division*
[2]*University of Maryland, College Park*

Introduction: Quantum information technologies, which include quantum communications and quantum computing, offer revolutionary opportunities for highly secure communications and for real-time processing of large data arrays in battle environments, which are important to the Department of Defense. The fundamental properties of quantum mechanics, such as entanglement and measurement-induced "collapse" of a quantum state, can prevent eavesdropping over quantum communication channels and can enable the solution of problems that grow exponentially difficult with classical computation.

Optical Spin Rotations: Electron spins in solids are among the leading candidates as quantum bits (qubits) for storage and processing of quantum information, with the direction of the spin — up or down — forming the two states of the qubit. The basic logic operation required for quantum information processing is the coherent rotation of the spin qubit. This is more general than simply changing the spin state from an initial prescribed state to a final one; instead, we need to be able to perform a given operation without knowledge of the input state of the qubit. This makes any protocol harder to design and implement. In our theoretical work,[1] we developed the design of a spin rotation protocol using fast optical laser pulses. This work provided a straightforward prescription for the experimental implementation of spin rotations, which had not been demonstrated at that time. This approach is fast and experimentally simple, and takes advantage of the special properties of optical pulses that have a hyperbolic secant temporal shape.

The spin can be represented by a 3D vector on a unit sphere (Bloch sphere), as shown in Fig. 4. Any rotation of a vector can be described by two quantities, the axis of rotation and the angle of rotation. A spin state that is parallel to the axis of rotation will not be rotated by said rotation, but in quantum mechanics it will acquire a phase. In the self-assembled III-V semiconductor quantum dots of interest in quantum information, there are preferred directions. The direction along which the quantum dot is grown sets the quantization axis for optical polarization selection rules. We use an external magnetic field to determine a second preferred direction, the energy quantization axis. To implement an arbitrary spin rotation, the two axes should not be parallel. We choose them to be orthogonal and refer to them as *z* and *x* respectively. We exploit the two inequivalent directions and, by adjusting the pulse polarization, induce phases to the corresponding spin states. This phase is precisely the angle of spin rotation.

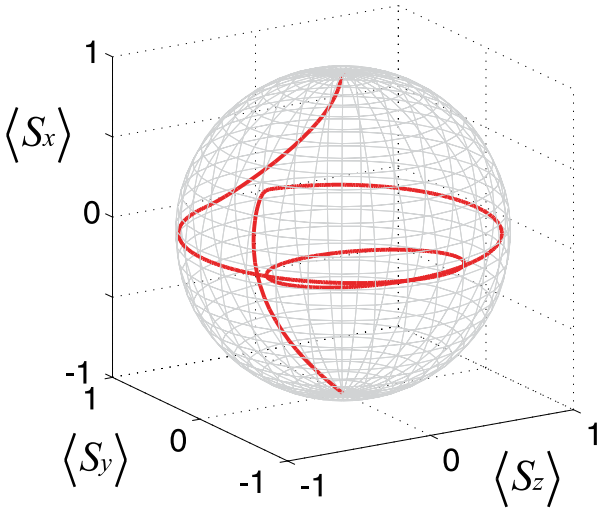

FIGURE 4
Calculation of the trajectory of the spin vector undergoing a rotation about the *y* axis composed of three rotations (*z*-*x*-*z*). The tip of the spin vector is shown (red).

The experimental demonstration of these ideas was carried out in our recent joint work with an experiment[2] on an ensemble of InAs quantum dots, each charged with an excess electron. A sequence of three pulses was used: a pump, a control, and a probe. The pump laser sets the spins in a well-defined initial state (z) perpendicular to the external magnetic field B, which points along the x axis. Under the influence of this magnetic field, the spins precess in the yz plane, as shown by the black line in Fig. 5(a). An appropriately chosen control laser pulse circularly polarized along the z axis will induce rotations of the spin about the z direction. Therefore, the effect of this rotation will be most evident when the control pulse finds the spin pointing along the y direction. The probe measures the z direction of the spin by optical absorption. Since the spin vector is precessing in a circle, its z projection will be oscillating in time, as shown in Fig. 5(b).

In the theory,[1] the angle of rotation depends on the detuning of the control pulse (the difference in optical frequency between the transition resonance and the pulse) for fixed pulse duration and pulse intensity. Thus only the control pulse frequency needs to be tuned in order to change the rotation angle. To demonstrate experimentally the predicted dependence of the spin rotation on the detuning, we fixed the intensity and time of incidence of the control pulse and varied the detuning. The measured z component of the spin is shown in Fig. 5(b) for several values of the detuning. The measured dependence of the rotation angle on the detuning is in very good agreement with the predicted one, as shown in Fig. 5(c).

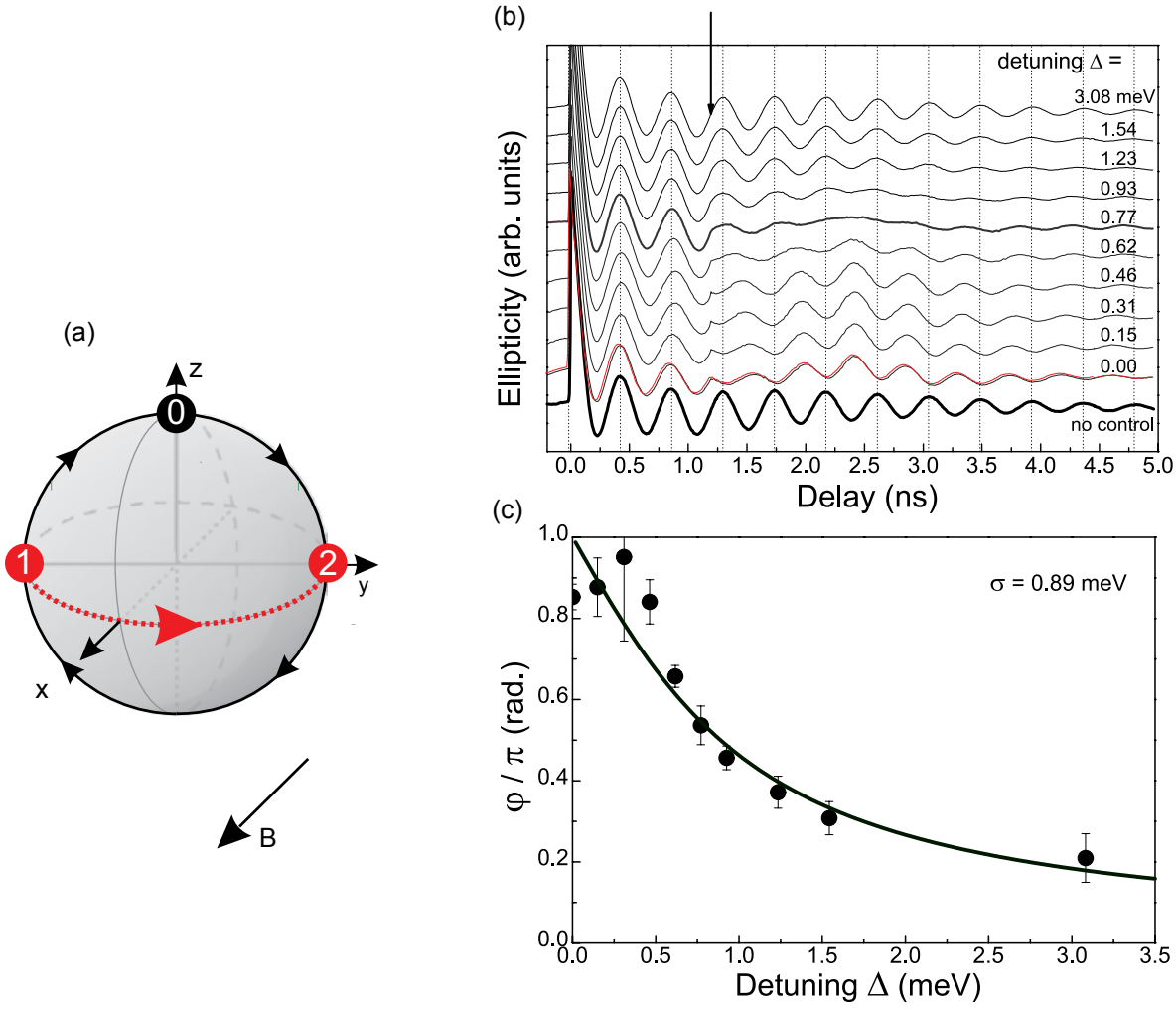

FIGURE 5
(a) Sketch of the spin vector tip precessing about the B field (x axis) and rotated about the z axis, from $-y$ to y. (b) Experimental data of the z projection of the spin as a function of time. The arrow denotes the time of incidence of the control pulse. The change in phase and amplitude of the z projection is due to the rotation of the spin. (c) Experimental dependence of rotation angle on the detuning of the control pulse (points) plotted against theoretical prediction (curve) with no adjustable parameters.

Conclusions: We have designed theoretically and demonstrated experimentally an optical technique to implement arbitrary spin rotations in semiconductor quantum dots. These single qubit gates form the fundamental logic operations in quantum information processing devices, which once built will have important implications for how the Navy processes information.

[Sponsored by NRL and ONR]

References

[1]S.E. Economou and T.L. Reinecke, "Thoery of Fast Optical Spin Rotation in a Quantum Dot Based on Geometric Phases and Trapped States," *Phys. Rev. Lett.* **99**, 217401 (2007).

[2]A. Greilich, S.E. Economou, S. Spatzek, D.R. Yakovlev, D. Reuter, A.D. Wieck, T.L. Reinecke, and M. Bayer, "Ultrafast Optical Rotations of Electron Spins in Quantum Dots," *Nature Physics* **5**, 262–266 (2009).

Sheet of Carbon Atoms Points Way to Ultra-fast Transistors

D.K. Gaskill, P.M. Campbell, G.G. Jernigan, J.B. Boos, J.G. Tischler, E.R. Glaser, J.C. Culbertson, J.L. Tedesco, R.L. Myers-Ward, C.R. Eddy, Jr., N.A. Papanicolaou, J.G. Champlain, D. Park, and R. Bass
Electronics Science and Technology Division

Introduction: Graphene is a two-dimensional sheet of carbon atoms arranged in a hexagonal pattern (similar to a "chicken-wire fence"), and due to its unusual properties is of great interest to the electronics community. For example, the electrons and holes in graphene act as if they have zero effective mass and travel at velocities faster than in any semiconductor. This property could be used to make a transistor that switches faster than any other made. Through a program in NRL's Institute for Nanoscience, researchers in the Electronics Science and Technology Division (ESTD) have developed a method to make wafer-scale graphene, known as epitaxial graphene (EG). These efforts resulted in NRL teaming with HRL, Inc., in DARPA's Carbon Electronics for RF Applications (CERA) program, where the team fabricated EG field effect transistors that defined the state of the art for graphene in several performance metrics. The characteristics of these devices have been used to predict that the ultimate switching speed of suitably scaled graphene transistors should be a trillionth of a second or faster. Such ultra-fast THz electronic devices are of great interest to the U.S. Navy for various applications, including low noise amplifiers (LNAs), where ultra-fast switch-ing cannot easily be achieved with existing electronics technology.

Epitaxial Graphene: For many years it has been known that heating silicon carbide (SiC) substrates to temperatures in excess of 1300 °C in ultra-high vacuum could sublime Si atoms, resulting in a carbon-rich surface. Recently, it has been understood that when this process takes place on the basal plane of hexagonal SiC, the residual carbon will reconstruct to form the graphene hexagonal lattice. NRL discovered that for improved graphene properties, the starting substrate surface must be prepared to be atomically smooth and free of underlying defects — this was achieved by etching the SiC substrate in hydrogen at elevated temperatures. After the subsequent sublimation of silicon, EG formation on the substrate surface was confirmed by graphene's relatively unique Raman spectral fingerprint. Figure 6 shows EG on the Si-polar face of a SiC substrate. Epitaxial graphene also grows on the C-polar face of SiC, albeit faster. Analysis of the film in Fig. 6 showed that the flat "terraces" between the raised "atomic steps" were covered with a single layer of graphene, about 3.3 Å thick, whereas the steps were covered with about two layers of graphene.

The electrical properties of EG were characterized by the van der Pauw Hall technique using small (10 by 10 μm^2) test structures. The 300 K Hall data for EG on the Si-face (blue) and C-face (red) of the SiC substrate are shown in Fig. 7. As can be seen, the mobility of graphene can be higher than that of conventional semiconductors, such as silicon. In addition, the data in Fig. 7 predict that EG will have extremely high

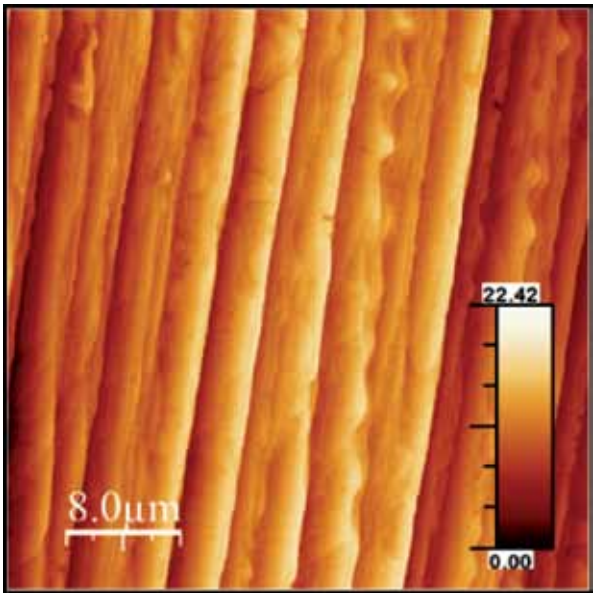

FIGURE 6
Atomic force micrograph of epitaxial graphene on the Si-face of SiC. The scale units are nm. The surface is dominated by terraces delineated by nearly vertical steps.

mobilities for low sheet charge densities, approaching 200,000 $cm^2\ V^{-1}s^{-1}$ for densities of $10^{11}\ cm^{-2}$.[1] To learn more about EG electrical transport properties, far-infrared magneto transmission (FIR-MT) measurements were carried out at 4 K. Absorption features are easily observed in the FIR-MT spectra and examples at various magnetic fields (B) are shown in Fig. 8. The strongest absorption feature (arrow) is due to a Landau level transition, $L_{-1(0)} \rightarrow L_{0(1)}$, that shifts in energy in proportion to the square root of B, as shown in the inset of Fig. 8. This square root dependence on B is consistent with carriers acting as if they have zero effective mass, one of the relatively unique properties of graphene.

In addition, the width of the absorption for different magnetic fields can be used to place a lower bound on the mobility of EG. Analysis of the line width of the strongest absorption feature showed that the sample contained regions with mobilities of at least 250,000 $cm^2\ V^{-1}s^{-1}$, a value consistent with the extrapolated value found in Fig. 7.[2]

The first EG experiments were carried out on small portions of SiC substrates and this later was transitioned to larger, wafer-sized samples. The critical parameter for graphene growth was the temperature uniformity across the "2-inch" (50.8 mm) diameter Si-face SiC wafers. Otherwise, EG was continuous

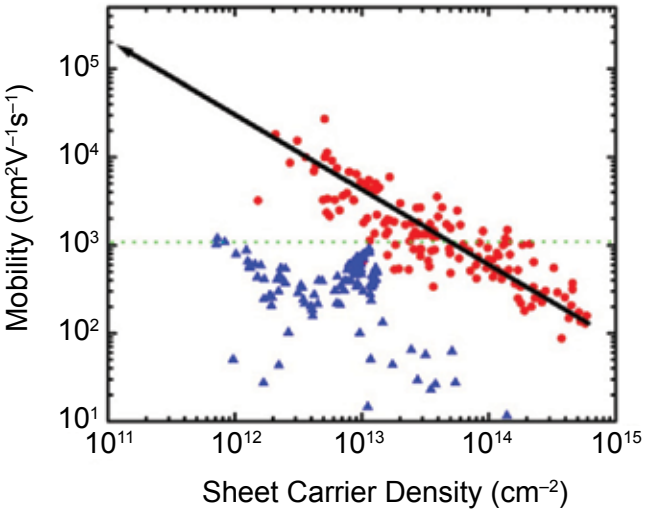

FIGURE 7
The 300 K mobility of 10 × 10 μm^2 van der Pauw Hall samples as a function of (single) sheet carrier concentration for EG on Si-face (blue) and on C-face (red) SiC. It can be observed that the values for C-face epitaxial graphene extrapolate to approximately 200,000 $cm^2\ V^{-1}\ s^{-1}$ for sheet density of $10^{11}\ cm^{-2}$ (black arrow). The dotted green curve marks the mobility of silicon.

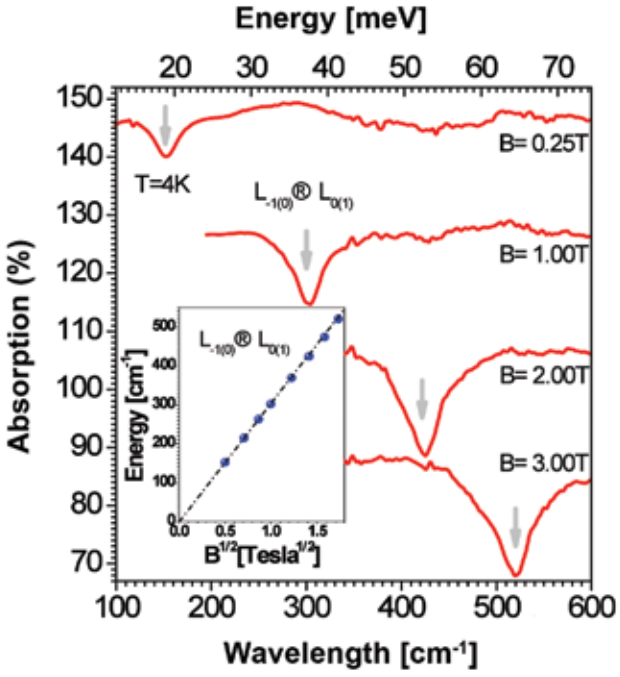

FIGURE 8
The far-infrared magneto transmission spectra of epitaxial graphene on C-face of SiC as a function of magnetic field B. The major absorption, denoted by the arrows, is due to Landau level transition, $L_{-1(0)} \rightarrow L_{0(1)}$. The absorption shifts in energy as the square root of B, shown in the inset, which is a characteristic of graphene and different from other semiconductors that shift linearly in B.

over the entire wafer with morphology similar to that shown in Fig. 6 and thicknesses as described earlier for the smaller samples.

Graphene Transistors: Another advantage of graphene is that silicon device fabrication techniques can be used with only minor modification to create graphene devices. This means that the etching, metallization, and dielectric gate deposition "tools" currently used in the silicon fabrication world can be employed to fabricate graphene devices. In addition, by using EG on wafers, literally dozens of experiments can be conducted at one time to optimize essential fabrication techniques. For these reasons, EG wafers provided by ESTD in collaboration with HRL in the CERA program quickly enabled significant progress in making graphene transistors. For example, wafers of this type yielded superior properties such as excellent resistivity uniformity of 2.8% and record 300 K Hall mobilities of ≈2700 $cm^2 V^{-1}s^{-1}$. Shown in Fig. 9 (top) is processed EG on a 2 in. diameter SiC wafer. Devices from EG wafers yielded field effect transistors exhibiting state-of-the-art ambipolar behavior, I_{on}/I_{off} ratios and peak transconductances.[3] Frequency performance metrics were established for these devices (L_g = 2 μm) such as cut-off frequency–gate length product ($f_T \cdot L_g$) of 10 GHz μm and f_{max} of 14 GHz. In addition, gate delay was found to be 2 ps μm^{-1}, which is very encouraging for superior high-speed gate-switching performance for small gate lengths.

ESTD recently began fabricating EG transistors and initial results yielded cut-off frequencies of 20 GHz for 130 nm gate lengths. A scanning electron micrograph of this device is shown in Fig. 9 (bottom). Although these speeds fall short of the expected potential of graphene-based transistors, this is an important first step along the path to create LNAs that reduce power consumption by a factor of six and increase the frequency of operation by a factor of two over existing state-of-the-art devices.

[Sponsored by ONR and DARPA]

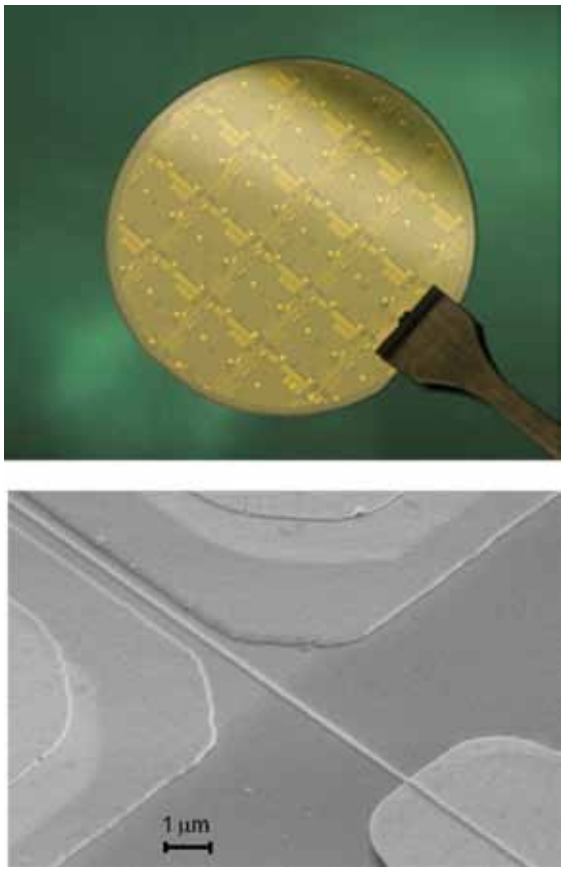

FIGURE 9
(Top) Epitaxial graphene processed into field effect transistors on a 50.8 mm diameter SiC wafer in collaboration with HRL, Inc., and in conjunction with the DARPA CERA program. (Bottom) Epitaxial graphene field effect transistor fabricated at ESTD. The gate length is 130 nm and the source–drain spacing is 1 μm.

References

[1] J.L.Tedesco, B.L. VanMil, R.L. Myers-Ward, J.M. McCrate, S.A. Kitt, P.M. Campbell, G.G. Jernigan, J.C. Culbertson, C.R. Eddy, Jr., and D.K. Gaskill, "Hall Effect Mobility of Epitaxial Graphene Grown on Silicon Carbide," *Appl. Phys. Lett.* **95**, 122102 (2009).

[2] G.G. Jernigan, B.L. VanMil, J.L. Tedesco, J.G. Tischler, E.R. Glaser, A. Davidson III, P.M. Campbell, and D.K. Gaskill, "Comparison of Epitaxial Graphene on Si-face and C-face 4H SiC Formed by Ultrahigh Vacuum and RF Furnace Production," *Nano Letters* **9**(7), 2605–2609 (2009).

[3] J.S. Moon, D. Curtis, M. Hu, D. Wong, C. McGuire, P.M. Campbell, G. Jernigan, J.L. Tedesco, B. VanMil, R. Myers-Ward, C. Eddy, Jr., and D.K. Gaskill, "Epitaxial-Graphene RF Field-Effect Transistors on Si-Face 6H-SiC Substrates," *IEEE Electron Device Lett.* **30**(6), 650–652 (2009).

Functionalized CMOS Nanomechanical Resonators for Chem-Bio Sensing

J.W. Baldwin, M. Zalalutdinov, J.S. Burgess, and B.H. Houston
Acoustics Division

Introduction: The canine olfactory system remains the most successful detector in use today for vapor sensing of explosives. For the lowest detectable concentrations (~1 ppb), in order to have a sufficient number of analyte molecules interacting with the olfactory neural receptors, the canine inhales as much as 10^{-12} to 10^{-13} g of analyte.[1] Our goal is to use arrays of low-cost complementary metal oxide semiconductor (CMOS) nanomechanical resonators with their extremely small mass and high surface/volume

ratio as a competitive and complementary technique for vapor sensing applications (i.e., for explosives, chemical warfare agents, and biomolecules). We have demonstrated that femtogram (fg) sensitivity, 10^{-15} g, is achievable in air under ambient conditions using functionalized CMOS nanomechanical resonators.[2] This research program has been focused on integrating nanomechanical resonators with all-electrical transduction in CMOS, essentially linking arrays of nanoelectromechanical-resonator systems (NEMS) with the information/signal processing capabilities of very large scale integration (VLSI) systems, and addressing the key outstanding problem of targeted functionalization.

A lack of selective functionalization on the resonator surface using vapor adsorptive functional groups specific towards target analyte molecules has been an impediment to the realization of resonator-based nanomechanical systems for mass sensing. When located on structural elements or microchannel walls, analyte-specific functional groups greatly limit the minimum detectable level of the overall device. In addition, traditional spin-cast polymer films used for preconcentrators and cantilever-based sensors present the problem of being many times thicker than the nanomechanical resonator, essentially burying the resonator in the adsorptive polymer. To address these problems, we use a monolayer functionalization scheme based on a UV-mediated reaction between terminal alkenes and a hydrogen terminated surface,[3] e.g., silicon or diamond, using a quartz mask to irradiate only the areas to be functionalized.

This ability to functionalize only the resonator and not the surroundings on a large scale is of great importance for attaining the highest sensitivity, and the monolayer functionalization technique maintains the high quality factor (Q) of the resonator. This opens the possibility of patterning arrays of NEMS, with each element having its own unique functional group, allowing for increased analyte selectivity for the overall device using a pattern recognition scheme. Moreover, we believe that the use of integrated arrays of such resonators, which according to current beliefs mimics the function of canine nose, enables an enhanced vapor sensing performance to be practically realized.

Design and Functionalization: The ideal resonator structure would have small mass, high quality factor, large surface area, and enough rigidity to withstand the wet chemistry processing associated with the surface functionalization. In order to be considered for field-type applications, the resonator sensor must have a built-in transduction mechanism, preferably an all-electrical operation. In this article, we present an arch-bridge resonator designed for integration with CMOS electronics and fabricated within an unmodified flow of a standard CMOS process.[2] The double-layer polysilicon (gate layer) is used as a structural material for the arch resonator, whereas the thermally grown field oxide serves as a sacrificial layer. The all-electrical operation of the arch resonator, shown in Fig. 10, is enabled by the thermoelastic excitation and piezoresistive readout of the mechanical vibrations.

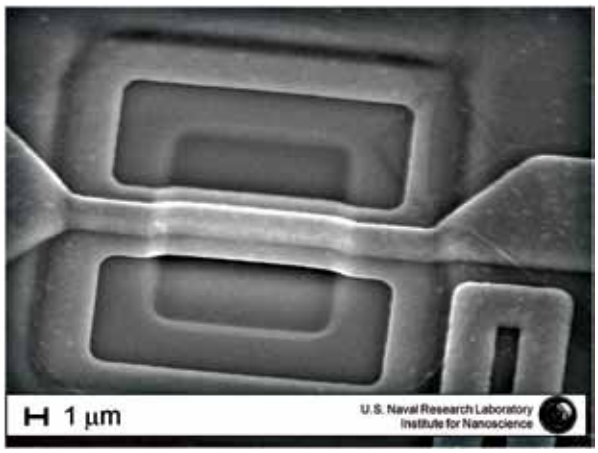

FIGURE 10
Arched bridge nanomechanical resonator with piezoresistive transduction and thermoelastic actuator implemented.

Figure 11 shows the reaction scheme for functionalizing the resonator with a hexafluoroisopropanol (HFIPA) group. The chip is first completely hydrogenated in a hydrogen plasma before contacting the surface with the terminal allyl. After contacting, a UV-transparent mask can be used to irradiate the features of interest, thus leaving the areas exposed to the UV light functionalized with the HFIPA group as seen in the X-ray photoelectron spectroscopy (XPS) spectra in Fig. 11.

Sensor Performance: The CMOS nanomechanical resonator in Fig. 10 was functionalized with the HFIPA group shown in Fig. 11 with no detectable degradation of the Q in air. A model analyte was chosen to show the hydrogen bond interaction between triethylamine (TEA) and the functionalized surface HFIPA, and to measure the level of detection that this device provides. Figure 12 shows the response of the resonator towards TEA, methanol, and water vapor. A mass flow controller (MFC)-controlled impinger, which delivers saturated vapor in nitrogen to a dilution chamber, is used to deliver the analyte vapor to the CMOS chip (5 by 5 mm) located in a flow cell (17 mL).

The plot in Fig. 12 was obtained by pulsing a single vapor at 100 standard cubic centimeters per minute (SCCM) for 2 min, 50 SCCM for 2 min, and 20 SCCM for 2 min, with a purge cycle of N_2 at 5 standard liters

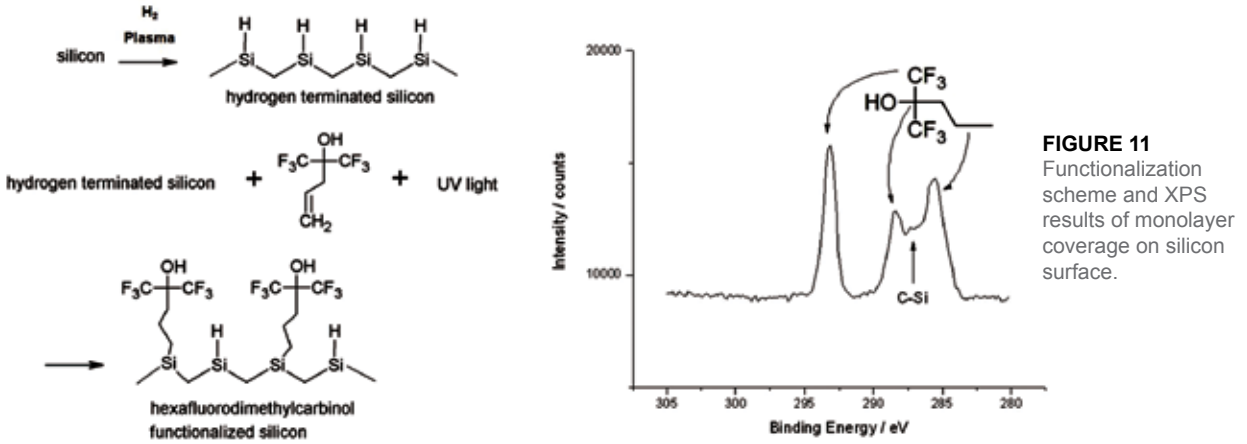

FIGURE 11
Functionalization scheme and XPS results of monolayer coverage on silicon surface.

per minute (SLM) for 2 min between each exposure. The process was repeated for each analyte individually (water 28‰, methanol 153‰, and TEA 69‰). No detectable adsorption of water and methanol was observed. The HFIPA functional group is hydrophobic due to the fluorination, and by design we would not expect physisorption of these two analytes. However, TEA is expected to hydrogen bond to the HFIPA group and is detected in our system. Adsorption was flow rate dependent. At 100 SCCM, 252 fg were adsorbed and detected, while at 20 SCCM, only 63 fg were detected. This shows the importance of using a microfluidic cell so that more analyte can be brought to the surface of the resonator in a shorter time.

The mass responsivity of this system (R) was estimated to be 1.26×10^{-18} g/Hz. A 1-fg detection level is projected for TEA, based upon the 1 kHz readout bandwidth. The resonator showed a selective response towards the TEA over typical solvent molecules.

Accomplishments: We have developed high-frequency and high-quality-factor NEMS resonator designs within commercially available, low-cost CMOS processes. These resonators have all-electrical drive and detection schemes incorporated into their design. We have accomplished the selective surface functionalization by depositing a vapor adsorptive monolayer of hexafluorodimethylcarbinol on nanomechanical resonators and measuring their response to various vapors. A 1-fg detection level was projected, based on the frequency stability of the resonator in air and the signal-to-noise ratio in the electromechanical transduction. The HFIPA-functionalized resonator showed a selective response to TEA over typical solvent molecules. We plan to expand the breadth of polymers specific to different analytes and to enhance the sensitivity levels by scaling down the dimensions of the resonators.

[Sponsored by ONR]

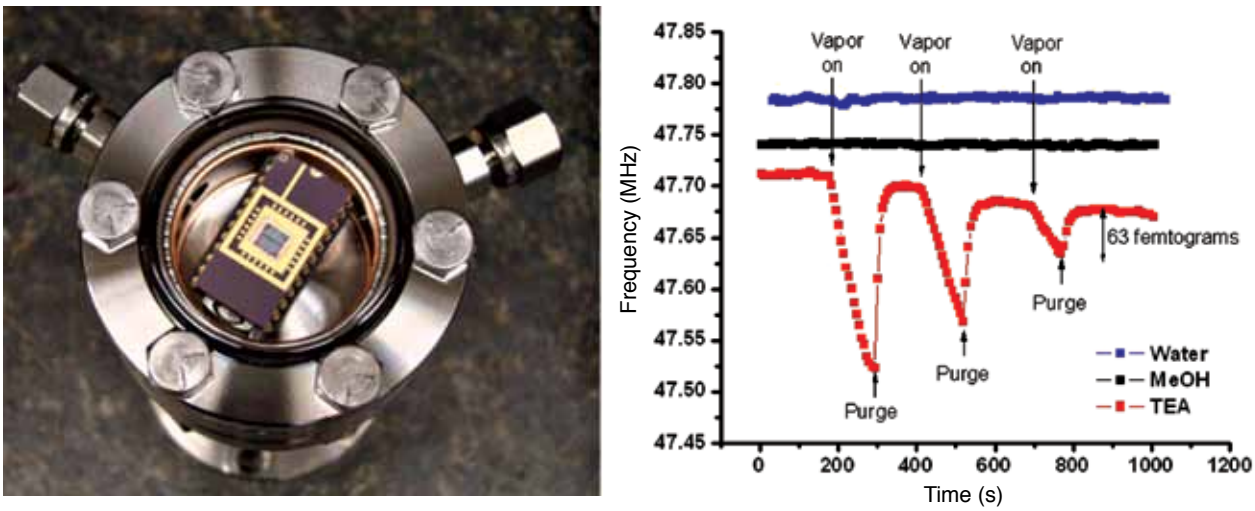

FIGURE 12
Prototype flow cell (left) with functionalized CMOS chip inside. Femtogram mass sensitivity and selectivity of triethylamine using functionalized arched bridge resonator (right).

References

[1] M. Krausa, and A.A. Reznev, eds., *Vapour and Trace Detection of Explosives for Anti-terrorism Purposes*, NATO Science Series II, Mathematics, Physics and Chemistry, V. 167 (Kluwer, Dordrecht, Netherlands, 2003).

[2] J.W. Baldwin, M.K. Zalalutdinov, B.B. Pate, and B.H. Houston, "Patterned Functionalization of Nanomechanical Resonators for Chemical Sensing," Navy Case Number 99,430, provisional application number 61/102,470; J.W. Baldwin, M.K. Zalalutdinov, B.B. Pate, M.J. Martin, and B.H. Houston, "Optically Defined Chemical Functionalization of Silicon Nanomechanical Resonators for Mass Sensing," *Nanotechnology* 2008, 8th IEEE Conference on Nanotechnology, Arlington, TX, 18–21 August 2008, pp. 139–142, doi:10.1109/NANO.2008.48; M.K. Zalalutdinov, J.D. Cross, J.W. Baldwin, B.R. Ilic, W. Zhou, B.H. Houston, and J.M. Parpia,"CMOS-Integrated RF MEMS Resonators," *Journal of Microelectromechanical Systems* **19**(4), 807–815(2010).

[3] M.R. Linford, P. Fenter, P.M. Eisenberger, and C.E.D. Chidsey, "Alkyl Monolayers on Silicon Prepared from 1-alkenes and Hydrogen-terminated Silicon," *J. Am. Chem. Soc.* **117**(11), 3145–3155 (1995); T. Strother, W. Cai, X. Zhao, R.J. Hamers, and L.M. Smith, "Synthesis and Characterization of DNA-modified Silicon (111) Surfaces," *J. Am. Chem. Soc.* **122**(6), 1205–1209 (2000).